JPEDAV (2007) 28:23–37
DOI: 10.1007/s11669-006-9001-x
1547-7037 ©ASM International

Atomistic Modeling of Multicomponent Systems

G. Bozzolo and J.E. Garcés

(Submitted October 12, 2006)

The need to accelerate materials design programs based on economical and efficient modeling techniques provides the framework for the introduction of approximations in otherwise rigorous theoretical schemes. Several quantum approximate methods have been introduced through the years, bringing new opportunities for the efficient understanding of complex multicomponent alloys at the atomic level. As a promising example of the role that these methods might have in the development of complex systems, in this work we discuss the Bozzolo-Ferrante-Smith (BFS) method for alloys and its application to a variety of multicomponent systems for a detailed analysis of their defect and phase structure and their properties. Examples include the study of the phase structure of new Ru-rich Ni-base superalloys, the role of multiple alloying additions in high temperature intermetallic alloys, and interfacial phenomena in nuclear materials, highlighting the benefits that can be obtained from introducing simple modeling techniques to the investigation of complex systems.

Keywords computational statistics, first principles, interdiffusion, intermetallics, metallic alloys, modeling, Monte Carlo simulations

1. Introduction

Nearly all advanced engineering materials include a number of alloying additions, each with a specific purpose. While the desired goals might differ for different materials, similar obstacles are found in every other case, leading to the need of not only understanding the individual role that each addition could have in the original system, but also the interactions between them and how they affect, change, and sometimes invalidate, their original purpose. Taking, for example, Ni-base superalloys, certain elements are added to promote the precipitation of the γ' fcc ordered phase. Others are added to solid-solution strengthen either the matrix phase or the γ' phase. Still other elements are used to enhance interfacial or grain boundary strength, and other additions are intended to promote superior environmental resistance against oxidation, sulfidation, or hot corrosion. In addition, there are elements that have a major effect on rupture strength, creep properties, or fatigue. The multidimensional space generated by the current compositions and the number of needed experimental iterations turn further experimental design into an expensive and time consuming task, while providing significantly less potential benefit as the alloy system matures.

In spite of the promising applications of any given material, it is not uncommon that multiple alloying additions may interact more strongly with each other than with the base alloy resulting, for example, in precipitation of a second phase that was never intended. This was the case during the evolution of Ni-base superalloys, where refractory elements meant as solid-solution strengthening agents of both matrix and γ' precipitates, when added at high levels, resulted in the precipitation of refractory-metal-rich topologically closed-packed phases, deleterious to the mechanical properties of these materials. Unfortunately, overcoming these problems is a lengthy and expensive process, with no guarantee of success. Advances in computing power, however, have enabled the growth of computational modeling as an ever more efficient way to supplement materials development programs, making it possible that modeling, as an integral part of the alloy design process, could yield unexpected and viable new alternatives. In any case, it is essential to develop tools that could help researchers make educated decisions when designing new experiments, diminishing the serendipitous character of materials design by providing necessary guidance and criteria during the research process.

Although *ab initio* or first-principles (FP) approaches provide the most accurate framework for such studies and to the problem of alloy phase stability, their substantial computational requirements still prevent these techniques from becoming economical predictive tools for systems as complex as most commercial structural or functional alloys. Alternative approaches exist, such as atomistic quantum

This article was presented at the Multi-Component Alloy Thermodynamics Symposium sponsored by the Alloy Phase Committee of the joint EMPMD/SMD of The Minerals, Metals, and Materials Society (TMS), held in San Antonio, Texas, March 12-16, 2006, to honor the 2006 William Hume-Rothery Award recipient, Professor W. Alan Oates of the University of Salford, UK. The symposium was organized by Y. Austin Chang of the University of Wisconsin, Madison, WI, Patrice Turchi of the Lawrence Livermore National Laboratory, Livermore, CA, and Rainer Schmid-Fetzer of the Technische Universitat Clausthal, Clauthal-Zellerfeld, Germany.

G. Bozzolo, Ohio Aerospace Institute, 22800 Cedar Point Rd, Cleveland, OH 44142, USA; **G. Bozzolo,** NASA Glenn Research Center, Cleveland, OH 44135, USA; **J.E. Garcés,** Centro Atómico Bariloche, CNEA, Bariloche 8400, Argentina. Contact e-mail: GuillermoBozzolo@oai.org

approximate techniques, that can handle simulations of more complex systems, in a more qualitative fashion than FP techniques. Besides the obvious gains in computational effort and data analysis, their main advantage is their ability to provide simple and basic interpretations of the phenomenon under study, relying on virtual concepts or processes via approximations, but associated to the mainstream concepts that characterize more realistic approaches.

The purpose of this work is to investigate one such approach, namely, the Bozzolo-Ferrante-Smith (BFS) method for alloys,[1] described in Section 2, and in order to demonstrate the depth and breadth to which this computational modeling technique can be used to study the behavior of complex alloys, four diverse applications are discussed in Section 3. In the first example, we examine a system which has recently become a promising line of research in the development of new superalloys due to the rather unexpected finding that the presence of Ru could lead to the formation of precipitates which meet the necessary requirements for which these materials are intended. In this case, the interaction between alloying additions adds to their individual role. In the second example, however, this is not the case: additions (Ti, Cu) to NiAl alloys change their individual behavior due to the interactions between them. A third example is included to demonstrate the ability of carrying the modeling program to high order systems, in this case a 5-element alloy. A final example deals with interfaces in nuclear fuels. One feature is common to these examples: the need to fully understand not just the individual behavior of each alloying element but also the system as a whole, which could only arise from a scheme where each element, whether in the majority or not, is described on an equal basis.

2. The BFS Method for Alloys

A fundamental understanding of materials requires a quantum mechanical description of the related solids and relies on the calculation of the corresponding electronic structure. Such calculations are mainly done within density functional theory (DFT), according to which the many-body problem of interacting electrons and nuclei is mapped onto a one-electron reference system (an ideal crystal) that leads to the same density as the real system. Simplifications are introduced without any particular reference to the system under study and no adjustable parameters appear in these methods. In essence, the BFS method follows a similar argument: substantial simplifications are made for the sake of simplicity, basically opting for replacing the real process of alloy formation by a virtual one with a minimal set of adjustable parameters. In the same way that DFT requires that the virtual system is a good representation of the real electron density, BFS is expected to reproduce the essential features of the equation of state of the solid at zero temperature and, in particular, around equilibrium. Thus, unlike *ab initio* methods that provide a full description of the system at hand (including band structure, density of states, charge density, etc.), BFS is limited to structural information that is, ultimately, contained in the binding energy curve describing the solid under study. If this description is correct, then the method should accurately reproduce the most critical properties of the solid in its final state, including the cohesive energy per atom, compressibility, and equilibrium Wigner-Seitz radius. As long as these properties are sufficient for an equally accurate description of defects, their accuracy is essential for addressing issues such as the site preference behavior of alloying additions in multicomponent systems, their phase structure, and interfacial phenomena.

The BFS parameters remain fixed and fully transferable for any case dealing with the same elements, regardless of their number, type, or structural bulk or surface properties. This restriction implies that in order for the method to be equally valid in a number of diverse situations, as DFT is, the parameters must contain all the information needed to warrant the accuracy of the virtual path chosen for describing the actual process of alloy formation. To this effect, the parameterization of the BFS method implies a somewhat different approach for the interaction between different atoms. In general, most approaches introduce some sort of interaction potential, with the parameters describing each constituent remaining unchanged in different applications. In BFS, it is precisely the set of parameters describing the pure element that is perturbed in order to account for the distortion introduced by the nearby presence of a different element or defect. Moreover, the additive nature of perturbation theory on which the method relies[1] results in that only information on the binary systems is needed for the parameterization of the method. Multicomponent systems are thus studied only via binary perturbations: the perturbation in the electron density in the vicinity of any given atom is computed as the superposition of individual effects due to each neighboring atom. This allows for an accurate but also computationally simple way to equally determine binary and higher order alloy properties and, in addition, easily detect general trends in multicomponent systems as are, for example, the systems presented in this work.

Basically, the BFS method provides a simple algorithm for the calculation of the energy of formation ΔH of an arbitrary alloy (the difference between the energy of the alloy and that of its individual constituents), written as the superposition of elemental contributions, ε_i , of all the atoms in the alloy, where ε_i denotes the difference in energy between a given atom in the equilibrium alloy and in an equilibrium single crystal of species i,

$$\Delta H = \sum_i \varepsilon_i \qquad \text{(Eq 1)}$$

In principle, the calculation of ΔH would simply imply computing the energy of each atom in its equilibrium pure crystal and the total energy in the alloy. In BFS, a two-step approach is introduced for the calculation of ε_i in order to identify contributions to the energy due to structural and compositional effects computed as isolated effects. Therefore, ε_i is broken up in separate contributions: (1) a strain energy (ε_i^S) that accounts for the change in energy due *only* to the change in geometrical environment of the crystal

lattice, ignoring the additional degree of freedom introduced by the varying atomic species in the alloy, (2) a chemical energy (ε_i^{C}), and (3) a chemical reference energy ($\varepsilon_i^{C_0}$), where these last two terms take into account the real chemical environment in the alloy and decoupling between structural and chemical effects, respectively. It is precisely in the BFS chemical energy where the set of parameters describing the pure element are perturbed in order to account for the distortion introduced by the nearby presence of a different element. While there is a certain level of arbitrariness in how this separation is implemented, it is only meaningful when a good representation of the initial and final states of the actual process is obtained by properly linking all contributions. This is achieved by recoupling the strain, chemical, and chemical reference contributions by means of a coupling function for each atom i, g_i, properly defined to provide the correct asymptotic behavior of the chemical energy. Summarizing, the contribution to the energy of formation of atom i is then

$$\varepsilon_i = \varepsilon_i^{S} + g_i\left(\varepsilon_i^{C} - \varepsilon_i^{C_0}\right) \qquad \text{(Eq 2)}$$

It can be shown that BFS predictions that result from this scheme are *identical* to FP calculations at or near equilibrium of the system under study.[2] To show this equivalence, we consider a multicomponent compound of X atoms in the unit cell. The energy of formation of an alloy, ΔH, is the difference between the total energy of the alloy and the sum of the equilibrium energy of each one of its components, E_X^0. In turn, the total energy of an alloy, E, can be written as the total energy of each of its components, ($E_{X,i}$), computed from the minimum of the universal binding energy relationship (UBER) of Rose et al.[3] (or any other equation of state at $T = 0$ K) and an 'alloying' term, $E_{residual}$. Combining these two definitions, we obtain

$$\Delta H = \sum_{X,i}\left(E_{X,i} - E_X^0\right) + E_{\text{residual}} \qquad \text{(Eq 3)}$$

This last expression can now be compared to the BFS expression for the energy of formation in terms of strain and chemical components, given in Eq 1 and Eq 2, reformatted to single out the energy contributions from monoatomic crystals:

$$\Delta H = \sum_{X,i} \varepsilon_{X,i}^{S} + \varepsilon_{\text{residual}} \qquad \text{(Eq 4)}$$

Thus, BFS extracts the maximum amount of information of a given compound from the single element UBERs, with $\varepsilon_{\text{residual}}$ responsible for any additional information regarding the mixing process. In BFS, this quantity is written as a linear combination of the coupling functions $g_{X,i}$ assigned to each atom i of element X ($X = A$, B):

$$\varepsilon_{\text{residual}} = \sum_{X,i} \mu_{X,i} g_{X,i} \qquad \text{(Eq 5)}$$

where, comparing with Eq 1, the constant coefficients μ are actually the so-called BFS chemical energies ε^{C}. Finally,

$$\Delta H - \sum_{X,i}\left(E_{X,i} - E_X^0\right) = \sum_{X,i} \varepsilon_{X,i}^{C} g_{X,i} \qquad \text{(Eq 6)}$$

The left-hand side of Eq 6 denotes quantities that can be properly described by FP-determined UBERs, whereas the right-hand side denotes a quantity that is exclusively computed within the context of BFS. If the method is meant to provide an accurate description of the mixing process and if the parameterization of the elements is properly included, then the validity of BFS is warranted when the identity between both terms is satisfied within the range of validity of the description of the system as provided by the UBER (i.e., in the vicinity of equilibrium). To illustrate this point, Fig. 1 displays results for several binary and higher order systems. The agreement between FP results obtained with the full potential Linearized Augmented Plane Wave method (LAPW)[4] and BFS predictions shown in Fig. 1 is the foundation for the quality of the results presented in this work.

In BFS, each one of the three virtual processes (strain, chemical, and chemical reference) is described, for each atom, by means of an equivalent crystal (EC), a virtual crystal whose bulk properties account for the distortion in the electron density around the reference atom. These distortions arise from structural defects (vacancies, local relaxations, interstitials, etc.) for the strain term, or changes in the nature of the chemical environment for the chemical terms. From a computational standpoint, the usefulness of the method relies on the simplicity of the calculations needed for the determination of the three EC associated with each atom i. The procedure involves the solution of a simple transcendental equation for the determination of the equilibrium Wigner-Seitz radius (r_{WSE}) of each EC, based on the Equivalent Crystal Theory (ECT) for solids.[5]

The BFS strain energy contribution, ε^{S}, is obtained by solving the ECT perturbation equation[6]

$$NR_1^p e^{-\alpha R_1} + MR_2^p e^{-(\alpha+1/\lambda)R_2} = \sum_k r_k^p \, e^{-(\alpha+S(r_k))r_k} \qquad \text{(Eq 7)}$$

while the BFS chemical energy is obtained by a similar procedure by solving the equation

$$NR_1^{p_i} e^{-\alpha_i R_1} + MR_2^{p_i} e^{-(\alpha_i+1/\lambda_i)R_2} = \sum_k r_1^{p_i} e^{-(\alpha_i+\Delta_{ki})r_1} + \sum_k r_2^{p_i} e^{-(\alpha_i+\Delta_{ki}+1/\lambda_i)r_2} \qquad \text{(Eq 8)}$$

where N and M are the number of nearest-neighbors (NN) and next-nearest neighbors (NNN) at distances R_1 and R_2 (in the equivalent crystal), respectively, r denotes the distance between the reference atom and its neighbors, and $S(r)$ describes a screening function. The sums run over all NN and NNN of the reference atom i. The EC associated with the chemical reference term is determined by solving Eq 8 and setting all the interaction parameters to zero (thus ensuring the absence of structural defects in the chemical part of Eq 2). These equations are written in terms of a small number of ECT parameters: p, l, α, and λ, describing each element i in its reference state (see Ref. 5 for definitions and details) and a matrix of perturbative parameters Δ_{ki}, which describe the changes in the electron density in the vicinity of atom k due to the presence of an atom k (of a different chemical species), in a neighboring

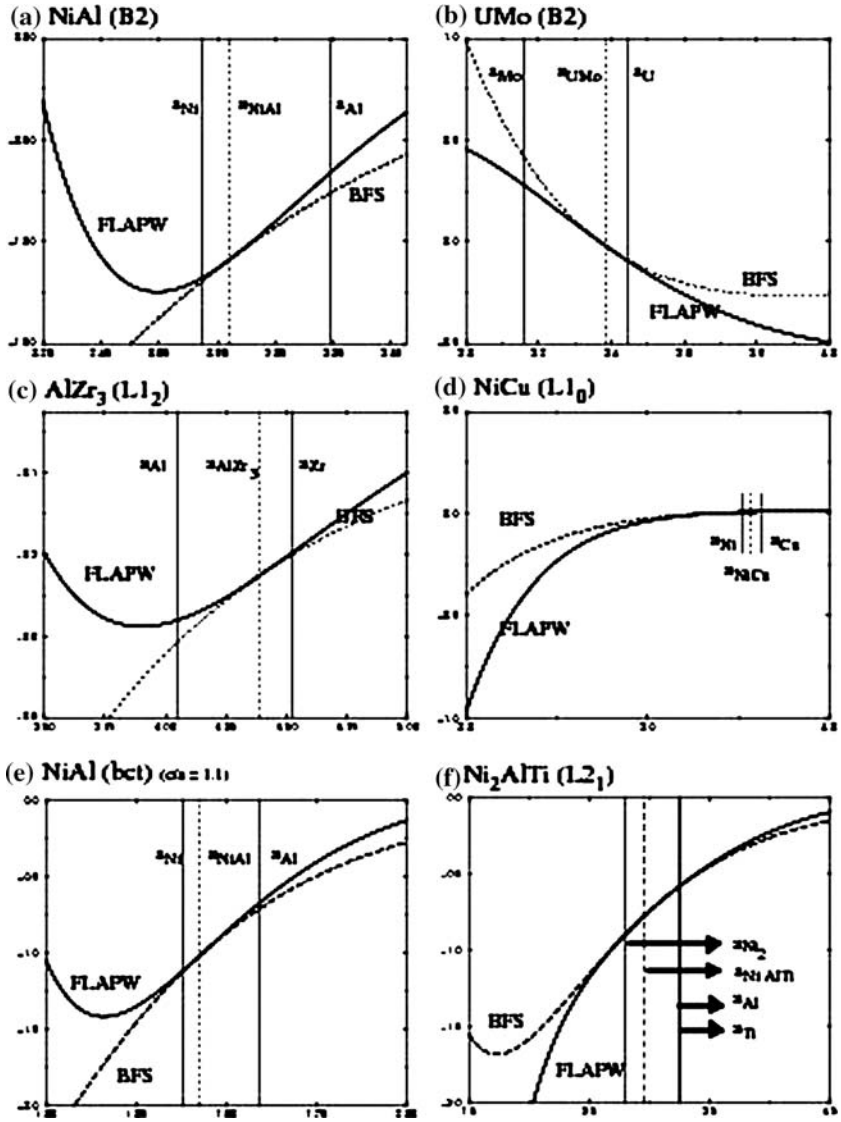

Fig. 1 Comparison of FP results (solid curves, in eV/atom) and BFS predictions (dashed lines), as described by Eq (6), and as a function of lattice parameter (in Å), for (a) NiAl (B2), (b) UMo (B2), (c) $AlZr_3$ ($L1_2$), (d) NiCu ($L1_0$), (e) body-centered tetragonal NiAl (c/a = 1.1), and (f) Ni_2AlTi ($L2_1$). In this last case, the Wigner-Seitz radius is used instead of the lattice parameter. The vertical lines denote the equilibrium lattice parameters of the individual elements (in the symmetry of the alloy, solid lines) and the lattice parameter of each ordered structure (dashed line), as predicted by FP methods

site. The primary set of parameters describing any arbitrary reference state for a given atom are related to the equilibrium values for r_{WSE}, the cohesive energy, E_c, and the bulk modulus, B_0, (or the scaling length l, used to replace B_0 in order to allow for a closer correspondence with the UBER). These equations are used for the calculation of the lattice parameter a^S or a^C for the strain and chemical EC, respectively, where the reference atom i has the same energy as it has in the geometrical environment of the alloy under study. Once the lattice parameter of the strain or chemical equivalent crystal are determined, the BFS contributions to the strain or chemical energy are computed using the UBER, which contains all the relevant information concerning a single-component system. Finally, as mentioned above, the BFS strain and chemical energy contributions are linked by a coupling function g_i, which describes the influence of the geometrical distribution of the surrounding atoms in relation to the chemical effects and is given by:

$$g_i = e^{-a_i^{S*}} \quad \text{(Eq 9)}$$

where the scaled lattice parameter in the exponent is given by

$$a_i^{S*} = q\frac{(a^S - a_i)}{l_i} \quad \text{(Eq 10)}$$

where $q = 3\sqrt{3/8\pi}$ for bcc and $q = 3\sqrt{3/16\pi}$ for fcc.

The BFS-based methodology assumes no *a priori* information on the system at hand and none of the experimental information that could be possibly available is used in the formulation and application of the method. The only input necessary consists of the lattice structures and the basic parameterization of the participating elements.

The BFS parameters are determined from FP calculations by using the LAPW method, as implemented in the WIEN2k package,[4] but their validation depends on their ability to describe basic known features of the binary combinations of these elements. For their verification and validation it is important to test the parameters against the generally abundant theoretical or experimental information, but the background available for some binary compounds is rather limited, as is the case with U-X compounds. Therefore, each application of BFS must include a thorough validation of the parameterization used. The parameters used in the examples shown in this work, as well as their validation and verification, can be found in Ref 6-11.

Throughout this work, a simple notation is used to indicate the possible substitution schemes: X(A) denotes an atom of species X occupying an A site. If the displaced A atom moves on to a neighboring site previously occupied by a B atom, the resulting defect is denoted as $X(A)A(B)_d$, where the subindex d distinguishes between the pair of defects (X(A) and A(B)) as being NN (d = 1), NNN (d = 2) or distances greater than that (either no subindex or $d = f$).

3. Results and Discussion

3.1 Modeling of RuAl-Based Multicomponent Alloys

In comparison with nickel or cobalt aluminides, B2 RuAl has appreciable room temperature toughness and plasticity, maintains considerable strength at high temperatures,[12,13] and has excellent oxidation resistance,[14] making this alloy a potential candidate for the challenging environments encountered in aerospace applications. To drive down cost and weight and improve upon its other properties, several studies[15-18] have looked at alloying schemes for replacing Ru or Al with other elements that generally form an isostructural B2 phase such as Co and Fe for Ru and Ti for Al. But by far, the most widely studied ternary alloying addition has been Ni,[19-29] although there is disagreement on the structure of ternary Ni-Ru-Al alloys that exist between the NiAl and RuAl B2-phase fields. Some studies[21-23,25,27-29] have reported a miscibility gap centered between the two binary phases resulting in a region consisting of two distinct B2 compounds, including a two-phase alloy at the composition $Ni_{25}Ru_{25}Al_{50}$.[23] Many, but not all, of the ternary compounds seemed to exhibit two distinct components, but the evidence seemed to suggest coring as opposed to actual formation of two distinct B2 phases.[24] Furthermore, a sample within the miscibility gap was heavily milled and annealed so that diffusion distances would be much smaller and a better opportunity for obtaining a near equilibrium structure would exist.[22] In this case, only a single B2 phase was observed. In contrast, a single B2 phase across the (NiRu)Al system was found in mechanically alloyed samples when Ni was varied between 10 and 25 at.%, indicating complete mutual solubility between NiAl and RuAl.[26]

For Ta additions, Feng et al.[30,31] demonstrated the existence of a Ru_2AlTa Heusler (H) phase, which is also an equilibrium component in certain Ni-base superalloys containing high levels of Ru. Interest in Ru-containing alloys is growing since Ru additions seem to improve the high-temperature properties of Ni-base superalloys.[32,33] A similar case can be made about the beneficial strengthening effects of fine H precipitates.[30-32,34] However, besides the recently reported H phase[30] and a single phase B2-ordered $Ru_{55}Al_{32}Ta_{13}$ alloy,[31] very little is known about the ternary Ru-Al-Ta phase diagram. The existence of these two ordered structures, in addition to the fact that the binary RuAl phase diagram does not show Ru-rich ordered phases, suggests that Ta plays an important role in stabilizing highly ordered phases in the Ru-Al-Ta system.

3.1.1 The Ru-Al System. A comparison between the LAPW values and other calculated and experimental values of the lattice parameter, cohesive energy, and bulk modulus for NiAl and RuAl raises the necessary confidence in the parameterization used,[7] which remains the same when the methodology is applied to higher order systems.

The B2 RuAl phase field was studied by considering a large number of possible computational cells defining various defect structures for off-stoichiometric compositions. Regardless of whether structural vacancies were included or not in this set of possible configurations, it was found that the RuAl phase is energetically unstable with respect to changes in stoichiometry, as shown in Fig. 2. For Ru-rich alloys, the lowest energy configurations correspond to substitutional alloys characterized by clustering of excess Ru atoms (as opposed to alternative ordered patterns). This can be explained in terms of the individual BFS contributions ε_i (i = Ru, Al) to the energy of formation of the

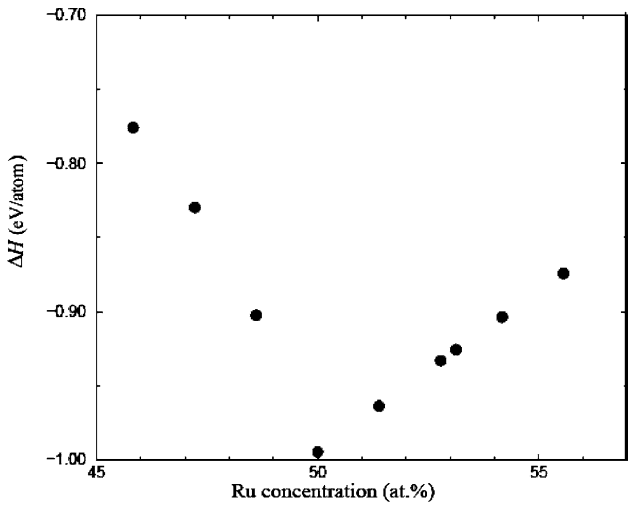

Fig. 2 Energy of formation of B2 RuAl (in eV/atom) vs. Ru concentration. The data points shown correspond to the lowest energy configuration found at each composition.

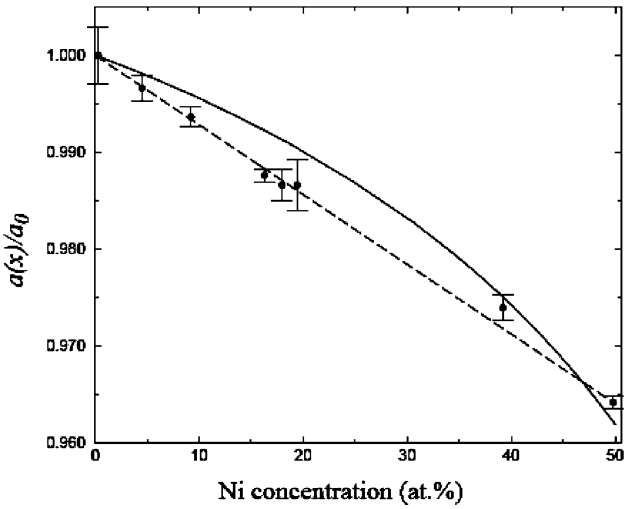

Fig. 3 Comparison of experimental results and BFS predictions (solid curve) for the lattice parameter of $(Ru_{50-x}Ni_x)Al_{50}$ alloys as a function of Ni concentration. The dashed line indicates the average values.

computational cell. For B2 RuAl, $\varepsilon_{Ru} = -0.34$ eV/atom and $\varepsilon_{Al} = -1.65$ eV/atom, indicating that both atoms contribute to the formation of the alloy (negative contributions to ΔH). The 'weak' contribution of Ru atoms (compared to that of Al atoms) and the similarity between the atomic volume per atom in the B2 RuAl alloy and the atomic volume in a pure Ru crystal, lead to the phase separation observed for Ru-rich alloys.[26]

3.1.2 The Ru-Al-Ni System. For the ternary case, the BFS values of the lattice parameter for $(Ru_{50-x}Ni_x)Al_{50}$ as a function of Ni concentration (in at.%), $a(x)$, show a slight deviation with respect to the average values, as illustrated in Fig. 3. Reported measurements[23,24] of $a(x)$ are also considered as having a linear behavior. The linear fit of the experimental values[23] (normalized to the equilibrium B2 value a_0) is $a(x)/a_0 = 1-0.0006949\ x$. In spite of the slight positive deviation from linearity, the best linear fit of the BFS prediction is almost identical, $a(x)/a_0 = 1-0.0007266x$.

We also studied the preferred site occupancy for dilute additions of Ni in RuAl. For $(Ru_{50-x}Ni_x)Al_{50}$ alloys, Ni(Ru) = −0.98 eV/atom and Ni(Al)Al(Ru) = −0.88 eV/atom, indicating that Ni prefers available Ru sites. However, for $Ru_{50}(Al_{50-x}Ni_x)$ alloys Ni(Al) = −0.96 eV/atom and Ni(Ru)Ru(Al) = −0.95 eV/atom, indicating a slight preference for Al sites, although the difference in energy is so small that it is difficult to conclude any obvious preference for either site under these conditions. The strong preference of Ni for Ru sites when Ni + Ru < 50 at.% is not surprising, as it allows for the formation of strong Ni-Al bonds.

Additional information can be obtained from the NN (or NNN) coordination matrices b_{ij} (or c_{ij}), shown in Table 1, which denote the probability that an atom i has an atom j as a NN (or NNN). While BFS-based simulations using the BANN algorithm[35] show the formation of the B2 RuAl phase, as can be seen in Fig. 4(a), the results are just

Table 1 NN (NNN) coordination matrices for the Ru-Al-Ni simulations shown in Fig. 4(b)

NN (NNN)	Ru	Al	Ni
Ru	0.000 (0.480)	0.992 (0.008)	0.008 (0.512)
Al	0.496 (0.004)	0.016 (0.985)	0.488 (0.011)
Ni	0.008 (0.512)	0.976 (0.023)	0.016 (0.465)

The matrix element in row i and column j denotes the probability that an atom of species i has a NN (NNN) of species j, where i (or j) = 1, 2, 3 correspond to Ru, Al, and Ni, respectively.

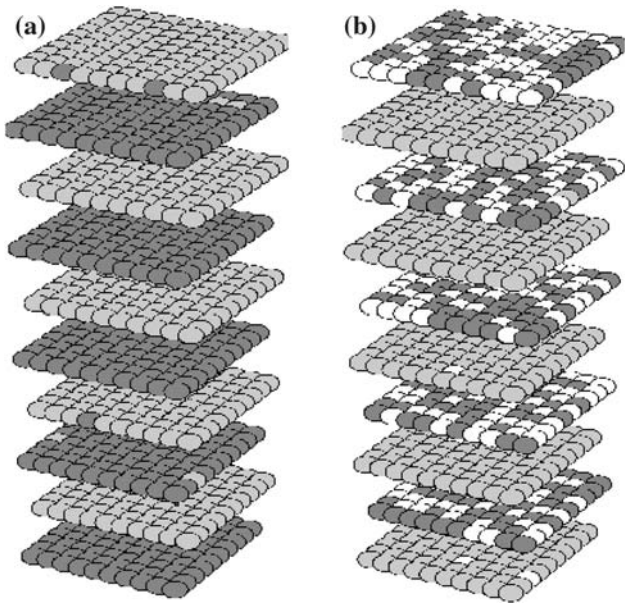

Fig. 4 Final state (room temperature) of BANN [35] simulations for (a) RuAl and (b) $Ni_{25}Ru_{25}Al_{50}$. Ni, Ru, and Al atoms are denoted with white, dark, and light gray spheres, respectively.

as clear for $Ni_{25}Ru_{25}Al_{50}$, as shown in Fig. 4(b). Both Ru and Ni share the same sublattice. If there is phase separation, it would be expected that atoms in the Ru/Ni sublattice will mostly have atoms of their same species as NNN. If there was a ternary ordered phase other than B2, the NNN coordination of Ru or Ni atoms would reflect this fact with an increasing number of NNN of the other species. For example, the NNN coordination matrix for a Heusler $L2_1$ ternary phase would maximize the value of $b_{NiRu}(= b_{RuNi} = 1)$. Phase separation, on the other hand, would lead to a very small value of b_{NiRu} (and b_{RuNi}), maximizing b_{NiNi} (and b_{RuRu}). Instead, the results of the simulations reflect the existence of a (Ru,Ni)Al B2 phase where Ru and Ni are randomly located throughout their own sublattice.[24,25]

More detail on the behavior or the ternary Ru-Al-Ni alloys regarding the role that each atom plays in $(Ru_{50-x}\ Ni_x)Al_{50}$ alloys as a function of Ni concentration can be obtained by separately computing the BFS energy contributions. Figure 5 shows the strain, chemical, and total energy

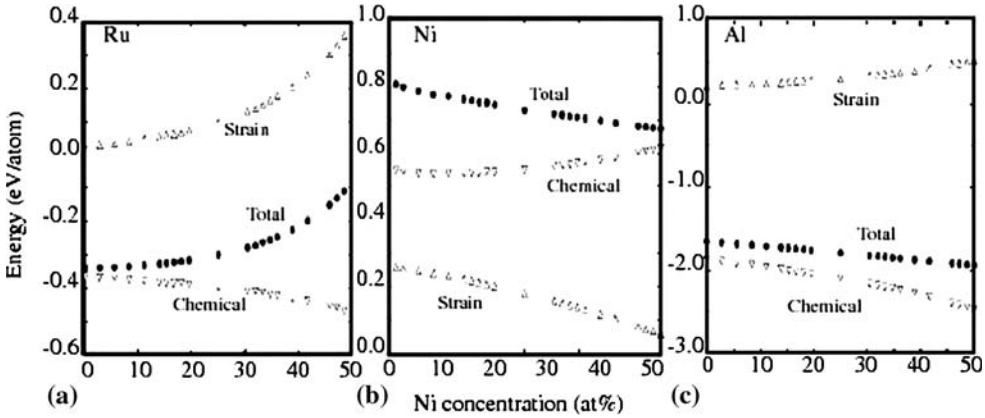

Fig. 5 Individual average BFS contributions for (a) Ru, (b) Ni, and (c) Al atoms in a $(Ru_{50-x}Ni_x)Al_{50}$ alloy, as a function of Ni concentration. In each case, the strain (up triangle), chemical (down triangle), and total (solid disk) energies are shown.

contributions of Ru, Ni, and Al atoms, computed as the average over all atoms of similar species. Ru atoms provide a favorable (i.e., $\varepsilon^C < 0$, favoring alloying) chemical contribution to the total energy of formation, diminished by increasing strain as the Ni concentration increases. As a result, the role of Ru in favoring compound formation is diminished with increasing Ni content (Fig. 5a). Ni atoms display the opposite behavior; as the concentration of Ni increases, the strain energy becomes substantially smaller as the average volume per atom in the alloy becomes closer to that of Ni. The chemical contribution (which does not favor alloying) increases, but at a slower rate than the decrease in strain, resulting in a total contribution that does not favor the stability of the alloy (Fig. 5b). Al atoms display a mild increase in strain with increasing Ni content, easily compensated by the growing chemical contribution (much more favorable than Ru), leading to a net decrease of the total energy (Fig. 5c), which along with the chemical contribution from Ru ultimately favors the formation of ternary B2 compounds.

While the modeling results are in agreement with some of the experimental evidence, it is expected that future experiments will clarify the uncertainties regarding the existence of a miscibility gap for this system.

3.1.3 The Ru-Al-Ta System. The site preference of Ta in $Ru_{50}(Al,Ta)_{50}$ alloys can be determined from two types of substitutions: (a) Ta occupying available Al sites, Ta(Al), (''direct'' substitutions) or (b) Ta occupying Ru sites, leading to the creation of additional antisite defects: Ta(Ru)Ru(Al). Direct substitutions, Ta(Al), lower the energy of the system, indicating an absolute site preference of Ta for Al sites. Configurations containing Ru(Al) antistructure atoms are much higher in energy due to the energy cost of creating antisite defects. This is detailed in Table 2, which displays the energy contributions of each substitutional atom and its immediate local environment to the total energy of formation. Relative to a homogeneous B2 RuAl cell, Ta(Al) substitutions lower the energy of the system by 1.44 eV/atom, while any other substitution raises the energy. The results could be understood as ranging from a very favorable situation for Ta in Al sites (which lowers the energy by 4.78 eV relative to an Al atom in that site), to a very unfavorable situation for the Al nearest-neighbors of Ta in a Ru site (which in the presence of Ta(Ru), collectively raise the energy by 10.56 eV relative to the case when a Ru atom occupies that site). Similar calculations for increasing number of Ta atoms show that the absolute Ta preference for Al sites in $Ru_{50}(Al,Ta)_{50}$ alloys is independent of concentration.

Table 2 Individual BFS contributions to the energy of formation (in eV/atom) of each non-equivalent atom for various substitutional defects, relative to a perfect B2 RuAl cell

Defect	Substitutional atom	NN(x8)	NNN(x6)	ΔE, in eV
Ta(Al)	−4.78 Ta(Al)	2.99 (Ru)	0.35 (Al)	−1.44
Ta(Ru)	0.88 Ta(Ru)	10.57 (Al)	0.06 (Ru)	11.50
Ru(Al)	1.68 Ru(Al)	0.81 (Ru)	−0.26 (Al)	2.23
Al(Ru)	10.56 Al(Ru)	6.13 (Al)	−0.01 (Ru)	6.67

Note: The first three columns show the total change in energy of the substitutional atom, the surrounding 8 NN and 6 NNN. The last column displays the net change in energy relative to B2 RuAl.

The role of Ta in stabilizing the ternary Heusler phase can be seen in the evolution of the energy of formation (per atom) of $Ru_{50}Ta_{50-x}Al_x$ alloys as a function of Ta concentration, as shown in Fig. 6, for the range $0 < x_{Ta} < 50$ at.%. Two distinct regimes can be seen: a low x_{Ta} regime, leading to the formation of the Heusler Ru_2AlTa structure (in the range $12.5 < x_{Ta} < 27.5$ at.%), in agreement with experiment,[31] and a high x_{Ta} regime where the energetics of the metastable B2 RuTa structure dominate.[36] The energy of formation (per atom) as a function of x_{Ta} shows increasingly large deviations from the average values for low x_{Ta}. For higher values, however, the ''average'' behavior is restored in a relatively linear fashion. The source for this behavior can be traced to the BFS contributions to the total energy of

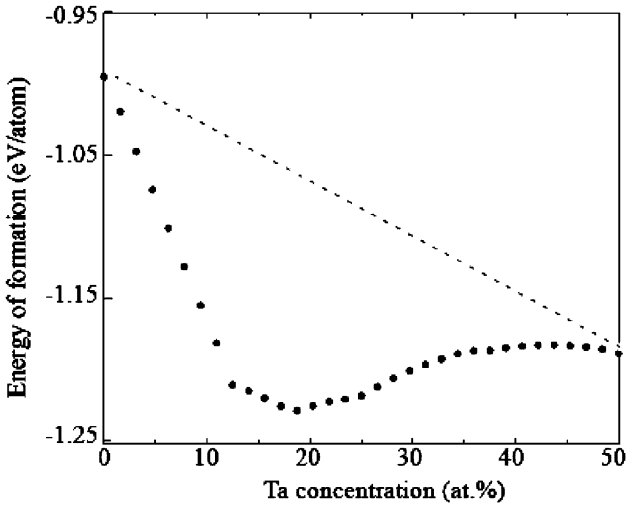

Fig. 6 Energy of formation (in eV/atom) of $Ru_{50}Al_{50-x}Ta_x$ ($0 < x < 50$ at.%) alloys as a function of Ta concentration. The data points shown correspond to the lowest energy configuration found at each composition by means of Monte Carlo simulations. The dashed line indicates the linear extrapolation from RuAl to RuTa.

Table 3 Individual BFS contributions to the energy of formation (in eV/atom) of each non-equivalent atom in B2 RuAl, $L2_1$ Ru_2AlTa, and B2 RuTa alloys

Alloy	Atom	E_{strain}, eV/atom	Coupling function	$E_{chemical}$, eV/atom	E_{total}, eV/atom
RuAl	Ru	0.03	1.09	−0.33	−0.34
	Al	0.23	1.38	−1.36	−1.65
Ru_2AlTa	Ru	0.01	0.95	1.41	1.35
	Al	0.10	1.25	−1.13	−1.31
	Ta	0.70	1.41	−4.93	−6.25
RuTa	Ru	0.11	0.82	3.89	3.31
	Ta	0.34	1.28	−4.71	−5.69

formation from each type of atom in RuAl, Ru_2AlTa, and RuTa, as displayed in Table 3. As mentioned above, the stability of the B2 RuAl structure (within the framework of BFS) is due to the fact that Ru and Al atom, have negative chemical energies, leading to the formation of strong bonds. Added to the low strain of Ru atoms in the equilibrium B2 cell, the contributions of Ru and Al atoms to the total energy of formation are negative (−0.34 and −1.65 eV, respectively), meaning that both favor alloying. The substitution of Al for Ta changes the balance, but not the end result: Ta plays a similar role as that of Al, in that Ta atoms provide strong negative chemical energy contributions. Increasing amounts of Ta, however, lead Ru to change its role. While the strain energy contribution of Ru atoms in Ru(Al,Ta) alloys continues to be small, the net contribution of each Ru atom to the energy of formation is now positive (1.35 and 3.31 eV in Ru_2AlTa and RuTa, respectively). The BFS results for Ru_2(Al,Ta) alloys show, in spite of Ru atoms "rejection" of Ta atoms as nearest-neighbors, a large negative contribution of Ta atoms, strong enough to offset increasing positive contributions from Ru atoms (unfavorable for alloying), leading to a highly stable $L2_1$ structure, as observed experimentally.[30] In contrast, the $Ru_{55}Al_{32}Ta_{13}$ alloy, was experimentally found to have a B2 structure with Ru-rich precipitates.[31] BFS results agree, showing also that the system does not undergo further ordering to a Heusler-type structure, retaining B2 Ru_{50}(Al,Ta)$_{50}$ order at any temperature.

3.1.4 The Ru-Al-Ta-Ni-W-Co-Re System. Finally, simulations can be extended to any alloy system regardless of the number of components. Monte Carlo simulations using BFS for the energetics,[35] were performed on a $Ru_{44.96}Al_{31.77}Ta_{12.92}Ni_{7.21}W_{2.01}Co_{1.01}Re_{0.11}$ alloy[30] equilibrated at different temperatures. Heusler ordering is observed below 1500 K. At lower temperatures, Ni atoms mostly occupy Ru sites, while Co, W and Re atoms reside primarily on Ta sites. The lattice parameter of the $T = 300$ K cell is 6.062 Å, just 0.5% smaller than the experimental value of 6.089 Å. At extremely low temperatures (below 100 K), the theoretical results indicate that solubility for W in the alloy is low and would lead to precipitation of some kind of W-rich compound.

3.2 Phase Structure of Multicomponent Systems

The lack of restrictions on the number of elements that can be included in any BFS modeling effort allows us to obtain valuable information on otherwise intractable systems in a straightforward fashion. A good example of this feature is a recent application dealing with the phase structure of a five element Ni-Al-Ti-Cr-Cu alloy, which was first predicted theoretically and later confirmed experimentally.[10] The process of modeling a multicomponent alloy starts with a detailed study of the defect structure as a function of stoichiometry for the base alloy,[37] B2 NiAl in this case, and continues with the analysis of the behavior resulting from the interactions of the different alloying additions with the base alloy and with each other. From this study, it was possible to determine some basic features of the ternary alloys Ni-Al + X (X = Ti, Cr, Cu): Ti was found to form ternary β′-Ni_2AlTi precipitates (Heusler phase, $L2_1$).[38] Cr, with a low solubility limit in NiAl, was found to form a bcc-Cr precipitate, and Cu, up to appreciable concentration levels, was predicted to remain in solid solution in the Ni-Al matrix.[39] The quaternary alloys are a good example of how to exploit the transferability of the parameters determined for each element and for each binary pair included in the quaternary system. The main objective is to identify possible changes in the behavior of each alloying addition due to the presence of the others. Ni-Al-Ti-Cu and Ni-Al-Ti-Cr alloys were therefore studied, focusing on the interactions between the alloying additions (Ti, Cu, and Cr). It was observed that, for the range of concentrations studied, none of the interactions between the alloying additions affected the previously observed behavior seen in the corresponding ternary systems.

Finally, large-scale simulations were performed on a five-element alloy ($Ni_{32.52}Al_{22.56}Ti_{9.47}Cr_{33.5}Cu_{1.95}$, in at.%),

chosen to capture previous observations such as Heusler (Ni_2AlTi) phase formation and Cr precipitation. Simulations on ternary and quaternary systems (leading to the pentalloy referenced above) showed little interaction between the different alloying additions. Supplemented with analytical calculations, the simulation results predicted the correct solubility limit for both the NiAl + Ti and NiAl + Cr systems. The correct structure of the second phase particles was predicted for both cases, as well as the lattice mismatch between the alloy matrix and the precipitating phases. In the quaternary alloy Ni-Al-Ti-Cu, the observed behavior did not differ from the one observed in the ternary cases, where Cu remains in solid solution in the NiAl matrix. It is in the case of the 5-element alloy that, surprisingly, a new feature was found, namely, the segregation of Cu to the NiAl/ α-Cr phase boundary. This is in contrast with the ternary examples (i.e., Ni-Al-Cu), where Cu remained in solid solution in the NiAl matrix.

After performing the large-scale simulations on the pentalloy, the alloy was cast and directionally solidified at a rate of 2.5 cm/h, thus creating a steep temperature gradient that is slowly traversed through the ingot. Figure 7 displays a bright-field TEM micrograph of the matrix phase as viewed in the [001] direction. The base NiAl alloy contains a high density of fine Ni_2AlTi (β') precipitates, resulting in the "tweed" contrast of the matrix. The alloy is also shown to contain a significant amount of lamellar α-Cr phase. Finally, Cu was found to partition to the β-NiAl/ β'-Ni_2AlTi phase in preference to the Cr phase. In addition, quantitative analysis of the Cr: $\beta + \beta'$ interface showed that there is an increase in Cu at the interface, consistent with the theoretical

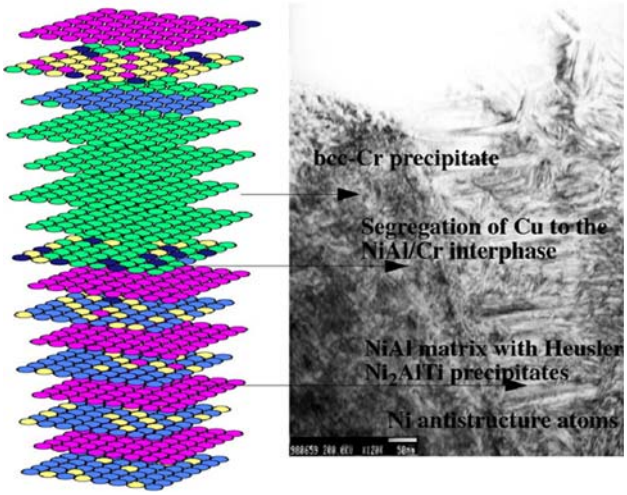

Fig. 7 BFS results for a $Ni_{32.52}Al_{22.56}Ti_{9.47}Cr_{33.5}Cu_{1.95}$ alloy, showing the final state at $T = 300$ K. Ni, Al, Ti, Cr and Cu atoms are represented with dark grey (red in online), medium grey (blue in online), white (yellow in online), light grey (green in online), and black circles (circles in online), respectively, represent the atoms. To the right of the simulation results, a low magnification TEM micrograph of NiAl-Ti-Cr-Cu directionally solidified alloy is shown. The matrix is oriented near the [001] zone axis and consists of a two-phase NiAl-Ni_2AlTi structure, which contains both coarse and extremely fine Cr precipitates.

prediction. Thus, by being able to study complex alloys theoretically as well as break the alloy down into simpler compositions, it is possible to understand in detail all the effects of various alloying additions on the structure of an alloy. This high resolution analysis capability of such complex systems is an essential ingredient of a virtual design process that allows the designer to investigate a broader range of alloy compositions and their properties than are customarily considered during development of new materials.

3.3 Site Preference Behavior in NiAlTiCu

Multicomponent modeling proved to be useful in the determination of fundamental behavior that demands detail difficult to obtain or just not accessible by experiment. One such example is the case of NiAl(TiCu) alloys where the site preference behavior for individual additions (Ti or Cu) is modified by the interaction between them. A recent[40] Atom Location by Channelling Enhanced Microanalysis (ALCHEMI)[41] study showed that the Cu content on Al sites is strongly dependent upon the stoichiometry of the alloy, whereas the Ti strongly prefers Al sites for all alloys. Five alloys were created as variations of the base composition $Ni_{50}Al_{47}Ti_3$ (at.%). In alloys No. 1, 2, and 3, the amount of Al replaced by Cu was 1, 3, and 6 at.%, respectively. Alloys No. 4 and 5 contain 1 and 3 at.% Cu, respectively, added to replace Ni. Transmission Electron Microscope (TEM) and Energy-Dispersive X-ray Spectroscopy (EDS) analysis on all five alloys resulted in the site occupancies for Ti and Cu shown in Fig. 8, along with the calculated uncertainties, and the BFS results.[6] The calculations not only reproduced the experimental results with a great deal of accuracy, as can be seen in Fig. 8, but a systematic analysis of the role of each addition and their interactions shed light on the role reversal of Cu, explaining why Cu substitutes for either Ni or Al sites, depending on stoichiometry. In brief, it was determined that the strong ordering tendencies of NiAl alloys, coupled with the strong preference of Ti for Al sites, as well as the less prominent interaction between Cu and Ti atoms and the small energy difference for Cu atoms in Ni versus Al sites, all contribute to make Cu atoms the ones most likely to fill in for any deficiency on either side of stoichiometry. This translates into a smooth transition from Al to Ni site occupancy as the change in composition becomes Ni-poor. The structure of the low-lying energy states (i.e., most likely to appear) and the energetics of individual atoms or groups of atoms, is summarized in Fig. 9. A reasonably large set of different atomic configurations in a 72-atom cell (sufficiently large to represent the most relevant distributions) is defined and its energy of formation computed using BFS. In what follows, we will use the notation $Ni_{[i]}Al_{[j]}Ti_{[k]}Cu_{[l]}$ to denote the concentration of the alloy in terms of the number of atoms in the 72-atom cell (e.g., $[i] = 36$ corresponds to 50 at.% Ni).

In order to match the compositions studied either experimentally or with Monte Carlo simulations as closely as possible, we define 25 compositions that properly cover the whole range of Ni, Al, and Cu concentrations studied before. These states correspond to alloys $Ni_{[A]}Al_{[B]}Ti_{[2]}$-

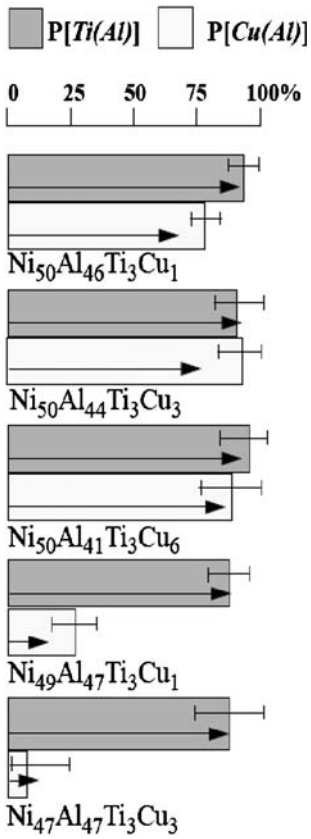

Fig. 8 Comparison of the occupation probabilities of a Ti or a Cu atom occupying a site in the Al sublattice (P[Ti(Al)] and P[Cu(Al)], respectively) from experiment (shaded rectangles), with the corresponding uncertainties. The BFS results are indicated with arrows.

$Cu_{[C]}$, where the subindex indicates the number of atoms of each species in the 72-atom cell ($A + B + C = 70$). For each concentration a catalog of configurations is built so that, if large enough, it will contain every possible arrangement of atoms that is likely to occur in the real alloy. We then compute the energy of formation of each cell so that energetically favored configurations can be identified. Visual examination of Fig. 9 provides an indication of the characteristic features of each region in the range of concentrations studied. The Ti-Cu ordering in the Al sublattice that characterizes alloys where $N_{Ni} > N_{Al}$ transitions to an intermediate regime where no specific pattern dominates ($N_{Ni} \sim N_{Al}$), to be replaced later by another ordering pattern in the Ni sublattice (Al-rich alloys) governed by Cu-Cu interactions.

While the top row of Fig. 9 highlights the role of the coupling series Cu(Al) ↔ Ti(Al) ↔ Ni(Al) in $Ni_{[37]}Al_{[34-x]}Ti_{[2]}Cu_{[x]}$, ($x$ = 1, ..., 5) alloys, the next rows are examples of the same coupling feature but without the Ni antistructure atom, indicating that it is precisely the presence of antisite defects and other substitutional atoms what ties substitutional Ti atoms together. Their absence, as in alloys with N_{Al} = 33 and N_{Al} = 34, result in Ti(Al) atoms remaining in solution. The set with N_{Ni} = 35 marks the transition between the Cu(Al) ↔ Ti(Al) ↔ Ni(Al) regime, characteristic of Ni-rich alloys, to the migration of Cu atoms to the Ni-sublattice that is dominant in Al-rich alloys. Finally, alloys with N_{Ni} = 33 and 34 transition to a regime where dominance of coupling between Cu atoms is the main feature. For example, $Ni_{[35]}Al_{[34]}Ti_{[2]}Cu_{[1]}$ represents the reduced importance of Cu-Ti coupling once Cu occupies Ni sites, while alloys with the same number of Ni atoms but increasing Cu content highlight the dual role of Cu linking Ti atoms when residing in Al sites and leading to Cu clustering when occupying sites in either sublattice. The NN bonds Cu(Ni)-Cu(Al) compete with Cu(Al) ↔ Ti(Al), thus

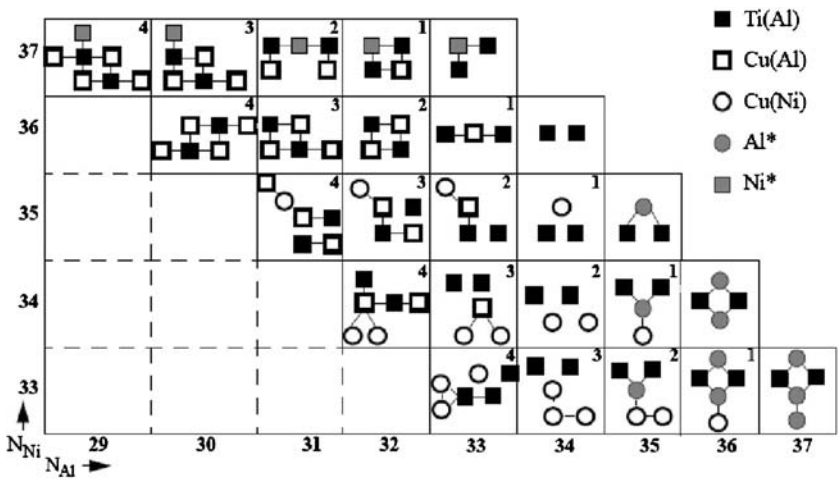

Fig. 9 Basic schemes of the ground state for each alloy modeled. Squares (circles) denote atoms in the Al(Ni) sublattice. Connected squares (circles) indicate NN bonds and isolated squares (circles) denote atoms that are separated by distances greater than NN distance. The ground state structures range from patterned Ti(Al) and Cu(Al) substitutions (upper left corner), to Ti(Al) and Cu(Ni) substitutions (lower right). Ni and Al content is indicated along the vertical and horizontal axes, respectively. Every configuration includes two Ti atoms and Cu is balance, as indicated by the number in the upper right corner of each box. Asterisks denote antistructure atoms.

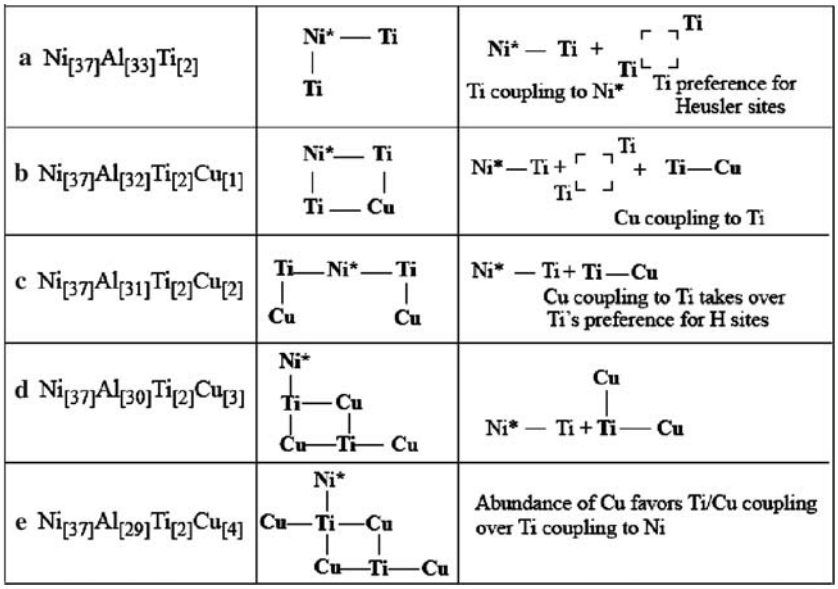

Fig. 10 Coupling series Cu ↔ Ti ↔ Ni, as manifested in Ni-rich alloys with increasing Cu content. The last column describes the individual elements, in order of importance, leading to the final state (center column).

explaining the small energy advantage of $Ni_{[35]}Al_{[33]}Ti_{[2]}Cu_{[2]}$ over a similar distribution where the isolated Ti atom is linked to both Cu(Al) and Cu(Ni), or, similarly, the advantage of $Ni_{[35]}Al_{[32]}Ti_{[2]}Cu_{[3]}$ over a similar configuration where the isolated Ti atom closes the square of NNN bonds between Ti(Al) and the two Cu(Al) atoms. After detailed numerical analysis,[9] Fig. 10 focus again on the relationship between the alloys studied experimentally and the modeling results, by describing the characteristics of the experimental cases and the relevance of the different effects identified by modeling.

3.4 Role of Si in the Diffusion of Al in UMo Fuels

This subsection highlights one of the basic questions in materials design, where basic simple systems need to be modified by means of alloying additions in order to meet strict specific properties for the application for which they are intended. As the number of alloying additions grows, it is inevitable to deal with secondary effects besides the individual role that each addition could have in the original system that affect, change, and sometimes invalidate, their original purpose. However, it is also possible that unexpected and viable new alternatives emerge. This is the case of additions to low enrichment uranium fuels (LEU, ^{235}U < 20 at.%) where the development of high density U-alloys with an increased concentration of U is one of the key problems for developing high neutron flux research reactors with LEU fuel.[42,43]

Among all intermetallic and uranium alloys, of particular interest is the U-Mo solid solution in the γ-phase dispersed in an Al matrix or in a monolithic form, which generated high expectation due to its acceptable irradiation behavior, low to moderate fuel/matrix interaction, and stable fission gas bubble growth for moderate neutron flux.[44-46] However, unexpected failures like pillowing and large porosities in LEU UMo dispersion plates and tubes in high neutron fluxes irradiation experiments have been reported.[47] These failures have been assigned to the formation of extensive porosity in the (Al,U,Mo) interaction product under high operating conditions.[48,49] As a consequence, the technological problem of developing LEU fuels remains open for suitable solutions as could be to modify the matrix or the UMo fuel by adding still unknown amounts of selected elements for changing the interaction layer and improve its irradiation behavior.

The complexities associated to this technological problem impose considerable demands on the traditional method for developing or improving specific alloys mostly based on extensive experimental trial and error work, which is both expensive and time-consuming. As is the case in most areas of modern materials science, it is only recently that the use of atomistic computational modeling in the development of structural materials has shown promise as a valuable tool to aid the experimental work, and to understand and predict the basic features that could be observed.

Experimentally, the Al/U interface is characterized by strong interdiffusion of both species and the formation of an intermetallic compound, mainly with the composition UAl_3. The BFS-based analysis indicates that the delicate balance driving Al interdiffusion can be greatly affected by the nearby presence of a different element in its neighborhood.

Denoting with $u_1, u_2, \ldots$ and $a_1, a_2, \ldots$ layers in the fuel or matrix side, respectively, going away from the interface, the BFS method allows for a detailed atom-by-atom analysis identifying the two main driving forces that control Al diffusion in the presence of Mo atoms in the Al/U-Mo interface: (a) the favorable configuration produced by the interchange $Al(a_1) \rightarrow Al(u_1)$ if there is an isolated $Mo(u_2)$ atom NN of the $Al(u_1)$, (b) the unfavorable situation for Al diffusion if there are $Mo(u_1)$ atoms as NN of $Al(a_1)$, and (c) the unfavorable situation produced by the increases of Mo

concentration in the solid solution. However, in spite of the fact that all the calculations refer to a rigid environment where both the Al matrix and UMo particles are represented by a bcc lattice characteristic of the UMo fuel, the basic features characterizing the real system can still be identified: (a) the increased Al/UMo interdiffusion with temperature, (b) the Al stopping power of increasing Mo concentration, (c) the formation of interfacial ternary compounds of varying composition, depending on their location relative to the interface, and (d) Al interdiffusion is prevalent in Mo-deficient regions of the U-Mo substrate.

The case of Si additions to Al induce a somewhat unexpected behavior by changing the role of the atoms present in the interface. There is no experimental evidence for this system. It is in cases like this where it is important to fill the knowledge gaps with modeling results that assure consistency with known cases. More importantly, analyzing every possible situation with the same modeling scheme allows us to gain detailed insight on the role played by each atomic species and the interactions between them. The conclusions that can be drawn through a BFS atom-by-atom analysis can be simply summarized by stating that Si plays the most important role in the Al-Si/U interfacial behavior by imposing a diffusion barrier, larger than that from Mo. Si also promotes cluster or compound formation in the interface.

Having shown that atom-by-atom calculations enable us to identify the driving forces for the observed experimental behavior, further information can be obtained from large-scale simulations with thousands of atoms, focusing on the behavior of the reaction layer. In spite of the rigid cell limitation in these simulations (based on a bcc cell with a lattice parameter characteristic of the U-Mo portion of the cell) it is possible to gather the necessary information to understand the behavior of Al in terms of Mo and Si concentration. The following set of simulations, depicted in Fig. 11, addresses the simultaneous effect of adding Si to Al

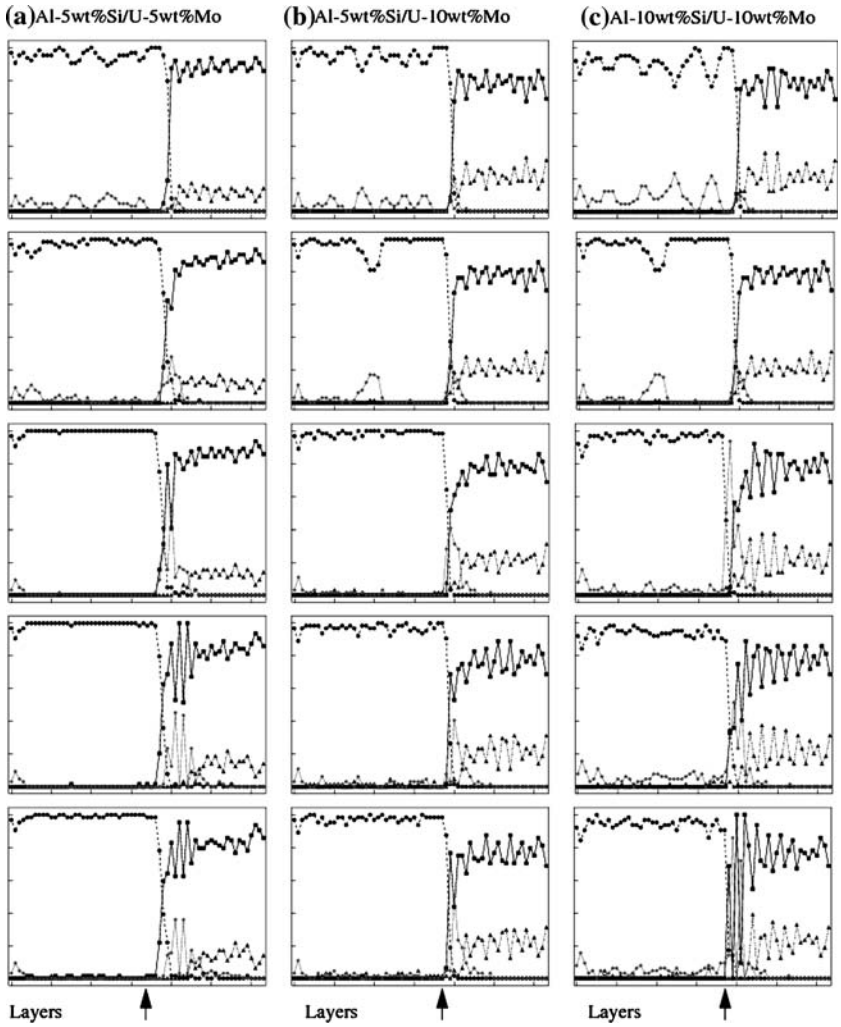

Fig. 11 Concentration profiles of the computational cells representing (a) the interfacial region between (a) Al-5 wt.% Si/U-5 wt.%Mo, (b) Al-5 wt.%Si/U-10 wt.%Mo, and (c) Al-10 wt.%Si/U-10 wt.%Mo. The profiles, from left to right, denote the changes in concentration (in at.%) in each plane in the vicinity of the interface. The different plots, from top to bottom, indicate the stable profiles at 90, 140, 190, 300, and 400 K, respectively. U and Mo profiles are indicated with black and gray solid lines, respectively. Al and Si profiles are indicated with black (dashed) and gray (dot-dashed) lines. The arrows indicate the location of the original interface.

and Mo to U, their influence in the structure of the interface, and in the interactions between the two alloying additions. The most striking result, a consequence of the interaction between all four elements, is the complete depletion of Si in Al regions close to the interface, an effect that is in excellent agreement with experiment. The simulation results for Al-5 wt.% Si and for Al-10 wt.% Si reproduce the main features of the experimental results, highlighting a strong trend towards the formation of interfacial compounds and much reduced diffusion of Al into UMo due to the high Si concentration. As mentioned earlier in this discussion, the limitation of working on a rigid bcc cell prevents us from properly determining the structure and composition of these compounds, but does not hinder the fact that their formation strongly depends on the Si and Mo contents. Additional effects due to the interactions between the participating elements are also observed. The most noticeable is the interaction between Mo and Si, resulting in a region free of Mo and Al where Si (in the majority) forms compounds. This effect, where Mo inhibits Si diffusion, is proportional to Mo concentration, allowing for Si-rich planes resulting in changes in the composition of the interfacial compounds from U_3Si to B2 USi. The combined effect of Si and Mo and their interactions is a noticeable decrease in Al diffusion, more noticeable with increasing content of either element.

To conclude this analysis, Fig. 12 compares experimental[50] and BFS-based results for Al-5.2 wt.% Si/U-7 wt.% Mo, showing a striking similarity between them: formation of Si precipitates far from the reaction layer, depletion of Si in the layers close to the interface, formation of interfacial compounds, and inhibited Al diffusion in the fuel.

Also, the role of another element, Ge, of the same group as Si, was investigated. In contrast with Si behavior, we observed a weak tendency to compound formation and, basically, no differences were observed in Al diffusion with respect to pure Al. As no experimental results or guiding evidence are available for the system Al-Ge/U-Mo, this is a good example of how computational modeling could help to understand the behavior of the system before proceeding to experimental verification.

4. Conclusions

The emerging trend of firmly connecting atomistic simulations, including first-principles-based electronic structure calculations, with the analysis of material properties has clearly helped in the development of new structural alloys or improving current alloys. The demands on the theoretical and numerical techniques used for that purpose have increased significantly, particularly in the ability of these methods to properly describe complex systems both in composition and structure. Combining first-principles methods with quantum approximate methods, as presented in this work describing the BFS method for alloys, has opened up new possibilities in the field of atomistic simulations, as they provide accurate and valuable input for the determination of parameters and their efficient use in computationally efficient methods. This approach is particularly useful when experimental data is not available and when the modeling results are part of the design process, where their

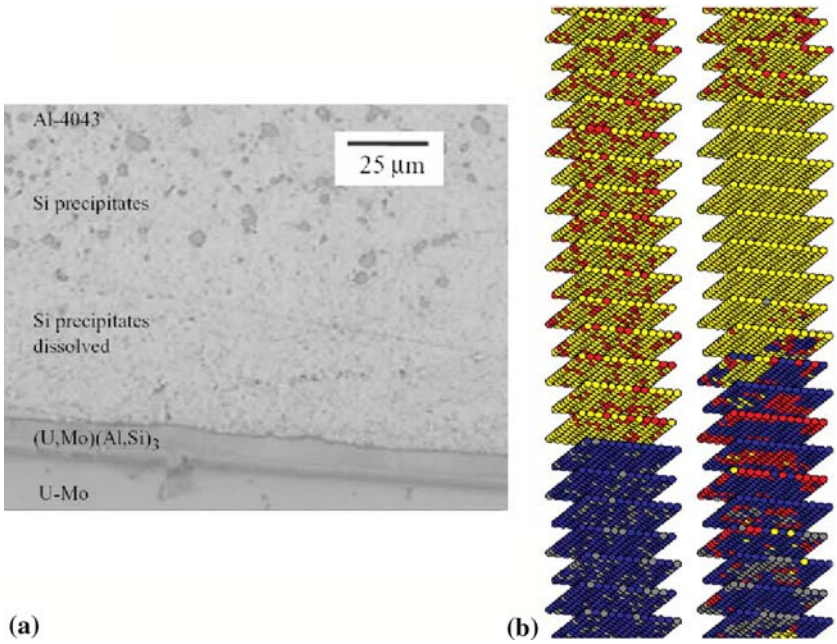

Fig. 12 (a) Al-5.2 wt.% Si/U-7 wt.% Mo interdiffusion layers showing the zone of depletion of Si precipitates near the interdiffusion layer.[50] (Reproduced with the permission of the authors). (b) Simulations of 64,000 atoms for Al-5.2 wt.%Si/U-7 wt.%Mo showing the main experimental results: Si depletion in Al side, the tendency to compound formation in the zone between Al and U-Mo sides and an unexpected interaction between Mo and Si which avoid the Si diffusion to deeper layers in the UMo solid solution thus improving the stopping power for Al diffusion.

predictive character is highly desirable. The method relies on first-principles-determined parameters with general transferability to broad situations, instead of parameters or potentials that have to be determined and optimized for each specific application, thus providing a simple framework for the analysis of multicomponent systems and their applicability for broad alloy design programs.

The particular way in which BFS models the process of alloy formation guarantees reliable results for bulk properties as well as for extended defects, surfaces, and interfaces, as detailed in the examples presented, which emphasize the fact that simple and straightforward descriptions of complex multicomponent systems is a reachable goal.

Acknowledgments

Discussions with N. Bozzolo are gratefully acknowledged. The authors also wish to thank H. Mosca, P. Gargano, G. Hofman, and J. Rest for their input. This work was sponsored by OAI/NASA Collaborative Agreement NNC05AA17A and supported by the NASA Fundamental Aeronautics Program.

References

1. G. Bozzolo and J.E. Garcés, Atomistic Modeling of Surface Alloys, *Surface Alloys and Alloy Surfaces, The Chemical Physics of Solid Surfaces*, Vol. 10, D.P. Woodruff, Ed., Elsevier, 2002, p 30-85
2. J.E. Garcés and G. Bozzolo, Determination of Structural Alloy Equilibrium Properties from Quantum Approximate Methods, *Phys. Rev. B*, 2005, **71**, p 134201-134210
3. J.H. Rose, J.R. Smith, and J. Ferrante, Universal Features of Bonding in Metals, *Phys. Rev. B*, 1983, **28**, p 1835-1845
4. P. Blaha, P.K. Schwarz, G.K.H. Madsen, D. Kvasnicka, and J. Luitz, *WIEN2k, An Augmented Plane Wave + Local Orbitals Program for Calculating Crystal Properties*, Karlheinz Schwarz, Techn. Universitat Wien, Austria, 2001. ISBN 3-9501031-1-2
5. J. Smith, T. Perry, A. Banerjea, J. Ferrante, and G. Bozzolo, Equivalent-crystal Theory of Metal and Semiconductor Surfaces and Defects, *Phys. Rev. B*, 1991, **44**, p 6444-6465
6. G. Bozzolo, R.D. Noebe, and J.E. Garcés, Atomistic Modeling of the Site Occupancy of Ti and Cu in NiAl, *Scripta Mater.*, 2000, **42**, p 403-408
7. P. Gargano, H. Mosca, G. Bozzolo, and R.D. Noebe, Scripta Metal. Atomistic Modeling of RuAl and (RuNi)Al Alloys, *Scripta Mater.*, 2003, **48**, p 695-700
8. P. Gargano, H. Mosca, G. Bozzolo, and R.D. Noebe, Atomistic Modeling of Ru-Al-Ta Alloys, *Scripta Mater.*, 2005, **52**, p 663-668
9. G. Bozzolo, H. Mosca, A. Wilson, R.D. Noebe, and J.E. Garces, Atomistic Modeling of Quaternary Alloys: Ti and Cu in NiAl, *Met. Trans. B*, 2002, **33**, p 265-284
10. A. Wilson, G. Bozzolo, R.D. Noebe, and J. Howe, Experimental Verification of the Theoretical Prediction of the Phase Structure of a Ni-Al-Ti-Cr-Cu Alloy, *Acta Mater.*, 2002, **50**, p 2787-2800
11. G. Bozzolo, J.E. Garcés, H. Mosca, P. Gargano, R.D. Noebe, and P. Abel, Quantum Approximate Methods for the Atomistic Modeling of Multicomponent Alloys, *Applied Computational Materials Modeling: Theory, Experiment, and Simulations*, G. Bozzolo, R. D. Noebe, and P. Abel, Ed., Springer, 2007, p 215-254
12. R.L. Fleischer, R.D. Field, and C.L. Briant, Mechanical Properties of High-temperature Alloys of AlRu, *Met. Trans. A*, 1991, **22**, p 403-415
13. R.L. Fleischer, Boron and Off-Stoichiometry Effects on the Strength and Ductility of AlRu, *Met. Trans. A*, 1993, **24**, p 227-230
14. R.L. Fleischer and D.W. McKee, Mechanical and Oxidation Properties of AlRu-Based High-Temperature Alloys, *Met. Trans. A*, 1993, **24**, p 759-763
15. R. Fleischer, Substitutional Solutes in AlRu I. Effects of Solute on Moduli, Lattice Parameters and Vacancy Production, *Acta Metall. Mater.*, 1993, **41**, p 863-869
16. R. Fleischer, Substitutional Solutes in AlRu II. Hardening and Correlations with Defect Structure, *Acta Metall. Mater.*, 1993, **41**, p 1197-1205
17. I.M. Wolff and G. Sauthoff, Role of an Intergranular Phase in RuAl with Substitutional Additions, *Acta Mater.*, 1997, **45**, p 2949-2970
18. S. Mi, S. Balanetskyy, and B. Grushko, A Study of the Al-Rich Part of the Al-Ru Alloy System, *Intermetallics*, 2003, **11**, p 643-650
19. I.M. Wolff and G. Sauthoff, Mechanical Properties of Ru-Ni-Al Alloys, *Metall. Mater. Trans. A*, 1996, **27**, p 1395-1400
20. I.M. Wolff and G. Sauthoff, High-temperature Behavior of Precious Metal Base Composites, *Metall. Mater. Trans. A*, 1996, **27**, p 2642-2652
21. S. Chakravorty and D.R.F. West, Phase Equilibria between NiAl and RuAl in the Ni-Al-Ru System, *Scripta Metall.*, 1985, **19**, p 1355-1360
22. S. Chakravorty and D.R.F. West, The Constitution of the Ni-Al-Ru System, *J. Mater. Sci.*, 1986, **21**, p 2721-2730
23. A.L.R. Sabariz and G. Taylor, Preparation, Structure and Mechanical Properties of RuAl and (Ru,Ni)Al Alloys, *Mater. Res. Soc. Symp. Proc.*, 1997, **460**, p 611-616
24. I.J. Horner, N. Hall, L.A. Cornish, M.J. Witcomb, M.B. Cortie, and T.D. Boniface, An Investigation of the B2 Phase between AlRu and AlNi in the Al-Ni-Ru Ternary System, *J. Alloys Compd.*, 1998, **264**, p 173-179
25. I. Vjunitsky, E. Schönfeld, T. Kaiser, W. Steurer, and V. Shklover, Study of Phase States and Oxidation of B2-based Al-Ni-Ru-M Alloys, *Intermetallics*, 2005, **13**, p 35-46
26. K.W. Liu, F.M. Muecklich, W. Pitschke, R. Birringer, and K. Wetzig, Formation of Nanocrystalline B2-Structured (Ru,Ni)Al in the Ternary Ru-Al-Ni System by Mechanical Alloying and its Thermal Stability, *Mater. Sci. Eng. A*, 2001, **313**, p 187-197
27. D. Hackenbracht and J. Kubler, Electronic, Magnetic and Cohesive Properties of Some Nickel-Aluminum Compounds, *J. Phys. F*, 1980, **10**, p 427-440
28. V.L. Moruzzi, A.R. Williams, and J.F. Janak, Electronic, Magnetic and Cohesive Properties of Some Nickel-Aluminium Compounds, *Phys. Rev. B*, 1974, **10**, p 4856-4862
29. A.R. Williams, J. Kuebler, and C.D. Gelatt Jr., Cohesive Properties of Metallic Compounds: Augmented-Spherical-Wave Calculations, *Phys. Rev. B*, 1979, **19**, p 6094-6118
30. Q. Feng, T.K. Nandy, and T.M. Pollock, Observation of a Ru-rich Heusler Phase in a Multicomponent Ni-Base Superalloy, *Scripta Mater.*, 2004, **50**, p 849-854
31. Q. Feng, T.K. Nandy, B. Tryon, and T.M. Pollock, Deformation of Ru-Al-Ta Ternary Alloys, *Intermetallics*, 2004, **12**, p 755-762

32. Q. Feng, T.K. Nandy, and T.M. Pollock, Solidification of High-Refractory Ruthenium-Containing Superalloys, *Acta Mater.*, 2003, **51**, p 269-284
33. A.P. Ofori, C.J. Rossouw, and C.J. Humphreys, Determining the Site Occupancy of Ru in the $L1_2$ Phase of a Ni-base Superalloy Using ALCHEMI, *Acta Mater.*, 2005, **53**, p 97-110
34. R.S. Polvani, W.S. Tzeng, and P.R. Strutt, High Temperature Creep in a Semi-Coherent NiAl-Ni_2AlTi Alloy, *Met. Trans. A*, 1976, **7**, p 33-40
35. G. Bozzolo, J. Khalil, and R.D. Noebe, Modeling of the Site Preference in Ternary B2-Ordered Ni-Al-Fe Alloys, *Comp. Mater. Sci.*, 2002, **24**, p 457-480
36. E. Raub, Die struktur der Festen Tantal-Ruthenium-Legierungen, *Z. Metall.*, 1963, **54**, p 451-459, in German
37. G. Bozzolo, R.D. Noebe, J. Ferrante, and A. Garg, Atomistic Simulations of Alloying Additions to NiAl, *Mater. Sci. Eng. A*, 1997, **239-240**, p 769-776
38. G. Bozzolo, R.D. Noebe, J. Ferrante, A. Garg, F. Honecy, and C. Amador, BFS Simulation and Experimental Analysis of the Effect of Ti Additions on the Structure of NiAl J, *Comput.-Aided Mater. Des.*, 1999, **6**, p 33-68
39. G. Bozzolo, R.D. Noebe, and C. Amador, Site Occupancy of Ternary Additions to B2 Alloys, *Intermetallics*, 2002, **8**, p 7-18
40. A. Wilson and J. Howe, Statistical Alchemi Study of the Site Occupancies of Ti and Cu in NiAl,, *Scripta Mater.*, 1999, **41**, p 327-332
41. I.M. Anderson, A.J. Duncan, and J. Bentley, Determination of Site Occupancies in Aluminide Intermetallics by ALCHEMI, *Mater. Res. Soc. Symp. Proc.*, 1995, **364**, p 443-448
42. CFR50, Limiting the Use of Highly Enriched Uranium in Domestically Licensed Research Reactors, *Federal Register*, **51**(377), 1986
43. J.L. Snelgrove, G.L. Hofman, M.K. Meyer, C.L. Trybus, and T.C. Wiencek, Development of Very-High-Density Low-Enriched-Uranium Fuels, *Nucl. Eng. Des.*, 1997, **178**, p 119-127
44. M.K. Meyer, G.L. Hofman, S.L. Hayes, C.R. Clark, T.C. Wiencek, J.L. Snelgrove, R.V. Strain, and K.-H. Kim, Low-Temperature Irradiation Behavior of Uranium Molybdenum Alloy Dispersion Fuel, *J. Nucl. Mater.*, 2002, **304**, p 221-236
45. D.B. Lee, K.H. Kim, and C.K. Kim, Thermal Compatibility Studies of Unirradiated U-Mo Alloys Dispersed in Aluminum, *J. Nucl. Mater.*, 1997, **250**, p 79-82
46. K.H. Kim, J. Park, C.K. Kim, G.L. Hofman, and M.K. Meyer, Irradiation Behavior of Atomized U-10 Wt.% Mo Alloy Aluminum Matrix Dispersion Fuel Meat at Low Temperature, *Nucl. Eng. Des.*, 2002, **211**, p 229-235
47. G. L. Hofman, M. R. Finlay, and Y. S. Kim, Post-Irradiation Analysis of Low Enriched UMo/Al Dispersion Fuel Miniplate Tests, RERTR-4 and 5, International Meeting on RERTR, November 7-12, Vienna, Austria, 2004
48. M.I. Mirandou, S.N. Balart, M. Ortiz, and M.S. Granovsky, Characterization of the Reaction Layer in U-7% Wt. Mo/Al Diffusion Couples, *J. Nucl. Mater.*, 2003, **323**, p 29-35
49. P. Lemoine, F. Huet, B. Guigon, C. Jarousse, and S. Guillot, French Development and Qualification Programs for the JHR Project Fuel Element, International Meeting on RERTR, November 7-12, Vienna, Austria, 2004
50. M. Mirandou, M. Granovsky, M. Ortiz, S. Balart, S. Aricó, and L. Gribaudo, Reaction Layer between U-7 Wt.% Mo and Al Alloys in Chemical Diffusion Couples, International Meeting on RERTR, November 7-12, Vienna, Austria, 2004